Journal of Materials Chemistry A

ROYAL SOCIETY OF CHEMISTRY

PAPER

View Article Online
View Journal

Cite this: DOI: 10.1039/d6ta02641a

Bridging crystalline MOFs with atomically dispersed metal–nitrogen–carbon catalysts *via* structure encoding

Daichi Homma,[a] Po-Wen Chung,[bcd] Shin R. Mukai[e] and Isao Ogino *[e]

Metal–organic frameworks (MOFs), and zeolitic imidazolate frameworks (ZIFs) in particular, have emerged as versatile precursors for metal–nitrogen–carbon (M–N–C) catalysts, in which atomically dispersed metal centers are coordinated by nitrogen within a carbon framework. Despite their widespread use, the mechanistic linkage between parent MOF structures and the catalysis-relevant properties of the derived carbons remains insufficiently defined. Here, using Fe–N–C catalysts for the oxygen reduction reaction (ORR) as a model system, we investigate how geometric factors inherent to ZIFs influence micropore formation, Fe–N_x site density, and electrochemical ORR performance. A geometric descriptor representing the linker-to-linker distance at the pore aperture, d_{L-L}, shows a stronger correlation with micropore volume than conventional pore descriptors such as the largest free sphere diameter (D_f) and largest included sphere diameter (D_i). The resulting micropore volume is further correlated with the density of formed Fe–N_x sites and ORR mass activity. As a practical validation, the Fe–N–C catalyst derived from MAF-6, identified by this descriptor-based selection, outperforms the widely used ZIF-8-derived analogue under polymer electrolyte fuel cell (PEFC) single-cell conditions, with approximately 1.5-fold higher mass activity at 0.8 $V_{iR\text{-free}}$. These results establish a structure–property–function relationship linking parent MOF structure, micropore evolution, Fe–N_x site formation, and ORR performance, enabling rational, high-throughput precursor selection from MOF databases.

Received 27th March 2026
Accepted 26th May 2026

DOI: 10.1039/d6ta02641a

rsc.li/materials-a

Introduction

Metal–organic frameworks (MOFs), and zeolitic imidazolate frameworks (ZIFs)[1] in particular, have emerged as versatile precursors for catalysts in which single metal atoms or metal clusters are coordinated by nitrogen within carbon matrices (metal–nitrogen–carbon, M–N–C).[2–14] Owing to their nitrogen-rich linkers and tunable crystalline frameworks, ZIFs enable the stabilization of isolated metal sites upon thermal conversion. Among these materials, Fe–N–C catalysts are promising platinum-free alternatives for the oxygen reduction reaction (ORR) in polymer electrolyte fuel cells (PEFCs);[5,6,8,10,14–22] however, precursor selection remains largely empirical, and a fundamental understanding of how catalysis-relevant carbon properties originate from parent MOF structures is still lacking. Despite the large structural diversity of ZIFs,[23,24] most prior studies have focused almost exclusively on ZIF-8,[2,4,7,8,14,19–22] which adopts the sodalite (sod) topology.[1]

Here, we introduce the concept of structure encoding, in which intrinsic geometric features of crystalline MOFs—such as characteristic length scales, framework topology, and connectivity—are transferred into the physicochemical properties of the resulting carbons during thermal transformation. In this framework, MOFs encode structural information that governs pore evolution, active-site formation, and catalytic performance. Using Fe–N–C catalysts derived from structurally distinct ZIFs as a model system, we demonstrate that geometric factors inherent to ZIF structures deterministically control micropore evolution and Fe–N_x site density, the key carbon descriptors that influence electrochemical performance under PEFC conditions. Correlating parent ZIF structures with carbon properties and ORR activity establishes a structure–property–function relationship that enables rational, high-throughput precursor selection for metal–N–C (M–N–C) catalysts.

To systematically probe structure encoding, we selected precursor frameworks based on crystallographic and geometric descriptors. Because nitrogen-containing linkers are essential for Fe–N–C synthesis, ZIFs incorporating imidazolate-based linkers were chosen. ZIFs consist of tetrahedrally coordinated metal cations (*e.g.*, Zn^{2+} or Co^{2+}) bridged by imidazolate linkers with a metal–linker–metal angle (~145°) closely matching the

[a]Graduate School of Chemical Sciences and Engineering, Hokkaido University, Sapporo, Hokkaido 060-8628, Japan
[b]Institute of Chemistry, Academia Sinica, Taipei 11529, Taiwan
[c]Department of Chemistry, National Taiwan University, Taipei 10617, Taiwan
[d]Department of Chemistry, National Sun Yat-sen University, Kaohsiung 80424, Taiwan
[e]Faculty of Engineering, Hokkaido University, Sapporo, Hokkaido 060-8628, Japan. E-mail: iogino@eng.hokudai.ac.jp

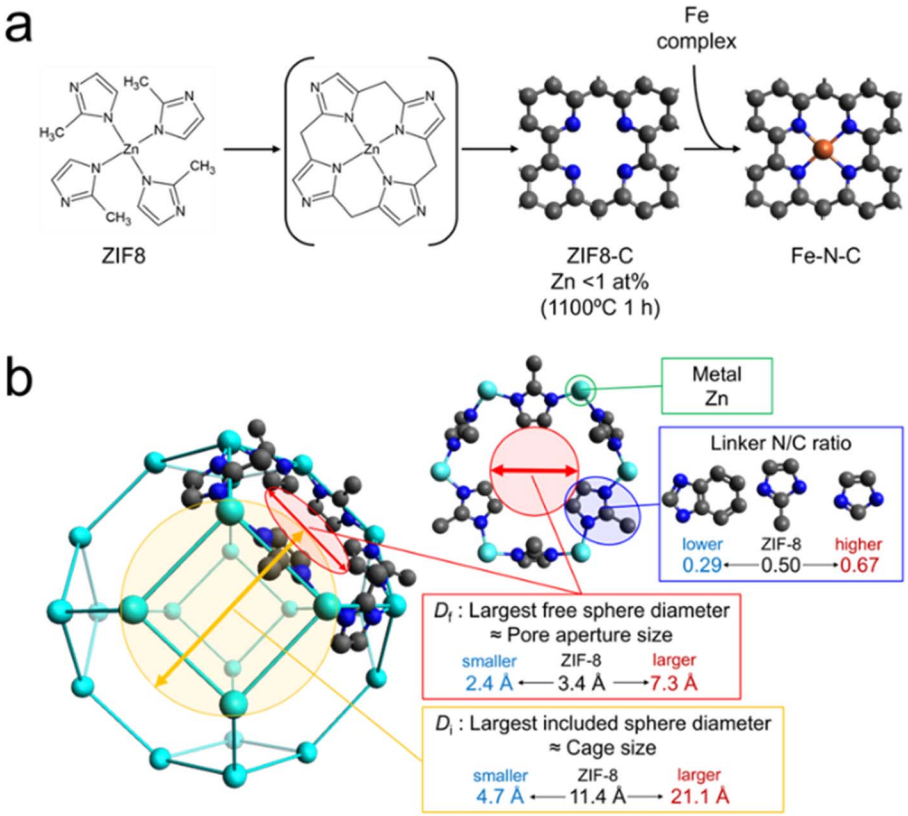

Fig. 1 (a) Schematic illustration of the synthesis of Fe–N–C catalysts from ZIF-8. The structure shown in the parenthesis represents a hypothetical structure.[26] (b) Three-dimensional structure of ZIFs and the structural descriptors considered in this study. Black, blue, cyan, and orange spheres represent carbon, nitrogen, zinc, and iron atoms, respectively.

Si–O–Si angle in zeolites, enabling zeolite-analogous topologies.[1,23] Substituents on imidazolate linkers influence the dihedral angle between adjacent linkers, thereby controlling framework curvature and ring size. Sterically unhindered linkers favor small-membered rings (*e.g.*, 6MR), whereas bulky substituents enforce larger rings with lower curvatures (*e.g.*, 8–12MR),[25] granting access to diverse topologies such as sod and rho.

Upon high-temperature pyrolysis, adjacent imidazolate linkers crosslink to form a continuous carbon framework,[26] while the fate of the metal nodes critically influences pore evolution. Co-based ZIFs tend to catalyze graphitization and pore collapse, whereas Zn-based ZIFs undergo Zn volatilization above ~900 °C, suppressing graphitization and preserving microporosity.[27] Accordingly, Zn-ZIFs pyrolyzed at 1100 °C yield highly microporous carbons that enable the formation of atomically dispersed M–N_x active sites (Fig. 1a).

We further hypothesized that linker identity governs both the porous structure of the parent MOF and the density of active sites in the resulting Fe–N–C catalysts through the nitrogen content of the linker. Based on this hypothesis, ZIF-8 was adopted as a reference framework, and a series of ZIFs incorporating linkers with systematically varied nitrogen-to-carbon (N/C) atomic ratios were selected. In addition, we posited that the intrinsic pore geometry of the parent MOF directly influences the microporous pore structure of the derived carbon, motivating our focus on two widely used geometric descriptors: the largest free sphere diameter (D_f) and the largest included sphere diameter (D_i) (Fig. 1b).[23] D_f quantifies the maximum pore aperture accessible to a spherical probe, whereas D_i represents the diameter of the largest cavity within the framework. The seven ZIFs investigated in this study (ZIF-4, ZIF-7, ZIF-8, ZIF-11, ZIF-71, ZIF-95, and MAF-6) were selected to span a wide range of N/C atomic ratios (0.29–0.67), pore aperture diameters D_f (2.40–7.32 Å), cavity diameters D_i (4.74–21.10 Å), ring sizes (6–12MR), and topologies (cag, sod, rho, poz) (Table S1), while sharing the common Zn-imidazolate precursor class.

By systematically varying linker chemistry and pore geometry across the selected MOF precursors and comparing the resulting Fe–N–C materials in terms of micropore volume and active site density (Fig. 1b), we sought to elucidate quantitative correlations between MOF structural descriptors and ORR catalytic performance.

Experimental

Synthesis of precursor MOFs

ZIF-4,[1] ZIF-7,[1] ZIF-8,[1] ZIF-11,[1] ZIF-71,[28] ZIF-95,[29] and MAF-6,[30] were synthesized according to the method reported procedures with slight modifications. Detailed synthetic procedures for each MOF are provided in the SI.

Pyrolysis of MOF-C and synthesis of Fe–N–C catalysts

MOF-derived carbons (MOF-C) and Fe–N–C catalysts were synthesized following the procedure reported by Wu *et al.*[31] The as-synthesized MOFs were pyrolyzed in a tubular furnace in flowing helium at 1100 °C (heat rate: 10 °C min^{-1}) for 1 h to obtain MOF-Cs. FE-SEM images characterizing before and after pyrolysis are provided in Fig. S3. For Fe incorporation, MOF-C (50 mg) was dispersed in 5 mL 2-propanol containing $FeCl_3 \cdot 6H_2O$ (4.15 mg). After solvent evaporation, the solid was thermally activated in flowing helium at 700 °C (heat rate: 20 °C min^{-1}) for 1 h to yield Fe–N–C catalysts, denoted as Fe-MOF-C.

Gas physisorption measurements

Ar adsorption measurements. Porous properties were characterized by argon physisorption at −187 °C (86 K) using an automated adsorption measurement system (Micromeritics 3Flex) at Academia Sinica. Prior to measurements, samples (≈60 mg) were degassed under vacuum at 250 °C for 4 h. Pore-size distributions were analyzed using two-dimensional non-local density functional theory with a heterogeneous surface model (2D-NLDFT-HS).[32] Microporous volume, V_{micro}, was calculated as the cumulative pore volume corresponding to pore width $W \leq 2$ nm.

N_2 adsorption measurements. Porous properties were also analyzed by nitrogen physisorption at −196 °C (77 K) using an automated adsorption measurement system (MicrotracBEL, BELSORP-mini) at Hokkaido University. Samples (≈20 mg) were degassed under vacuum at 250 °C for 4 h. For comparison purposes, the micropore volume was estimated from the amount of nitrogen adsorbed at a relative pressure of $p/p_0 = 0.1$, assuming complete pore filling by liquid nitrogen. The adsorbed amount was converted to an equivalent liquid volume using the density of liquid nitrogen (0.809 g cm^{-3}). This method provides a semi-quantitative approximation and was used only for a cross-instrument consistency check (Fig. S6 in the SI).

X-ray photoelectron spectroscopy (XPS)

X-ray photoelectron spectroscopy was performed on a JEOL JPS-9200 spectrometer employing a Mg Kα radiation (1253.6 eV) operating at 100 W and a pressure ~10^{-6} Pa. Samples were pressed onto an indium foil (99.99%, NILACO). The binding energy (BE) scale was calibrated using the C 1s peak at 284.8 eV. Survey spectra (0–1100 eV) were collected using a pass energy of 50 eV and a step size of 1 eV. High-energy resolution spectra were acquired using a pass energy of 10 eV with a step size of 0.1 eV. A Shirley background was applied for quantification of surface elements. Each N 1s spectrum was deconvoluted into three spectral components corresponding to pyridinic N at 398.5 eV, pyrrolic N at 400.1 eV, and graphitic N at 401.1 eV. Peak fitting was performed using a linear combination of Gaussian and Lorentzian functions with a fixed Gaussian–Lorentzian mixing ratio of 0.7. The FWHM was restricted to 1.6 eV for all components, and the relative peak positions were constrained during the fitting process.

Electrochemical quantification of Fe–N_x site density (SD)

The density of Fe–N_x sites was quantified using electrochemical stripping of NO derived from nitrite (NO_2^-).[4,33] Prior to measurement, catalyst powders were vacuum-dried at 80 °C for more than 12 h in a vacuum oven to remove physisorbed water and other volatile impurities. Catalyst inks were prepared by dispersing 2 mg of dried sample in a mixed solution consisting of 208 μL of distilled water, 208 μL of 2-propanol (99.7%, FUJIFILM Wako), and 21.6 μL of 5 wt% Nafion solution (Fujifilm Wako; 1-propanol 48 ± 3 wt%, water 45 ± 3 wt%, ethanol <4 wt%). The mixture was placed in an Eppendorf tube and ultrasonicated at 120 kHz for 30–60 min in an ice-water bath. A glassy carbon rotating disk electrode (BAS, Catalog number 013491, diameter 5 mm) was used as the working electrode (WE). The electrode surface was polished using a 0.05 μm alumina suspension on a polishing pad, followed by additional polishing with a clean, slurry-free pad. The polished electrode was mounted onto a rotating electrode apparatus (BAS, RRDE-3A) in an inverted configuration and rotated at 500 rpm during ink deposition. An aliquot of the prepared ink was drop-cast onto the electrode surface to achieve a loading of 0.2 mg cm^{-2}. After deposition, the electrode was dried at room temperature to form a uniform catalyst film. Electrochemical measurements were performed in a standard three-electrode cell (BAS) containing 70 mL of an acetate buffer at a pH of 5.2. An Ag/AgCl electrode (BAS, RE-1CP) and a Pt wire electrode (NILACO, 0.20 mm) were used as the reference and counter electrodes, respectively. To clean the catalyst film electrochemically, pretreatment CVs were performed between −0.4 and 1.05 V *vs.* RHE in the following sequence: (a) 3 cycles under O_2 at 5 mV s^{-1}, (b) 20 cycles under N_2 at 100 mV s^{-1}, (c) 10 cycles under N_2 at 10 mV s^{-1}, followed by repeating (a)–(c) and a final treatment identical to (a).

After cleaning, two types of background measurements were performed: (1) pre-baseline CV under N_2 (2 cycles, 10 mV s^{-1}, between 1.00 and 0.30 V *vs.* RHE), and (2) baseline CV under N_2 (2 cycles, 10 mV s^{-1}, between 0.40 and −0.30 V *vs.* RHE). These CV measurements were recorded immediately, serving as the unpoisoned reference. Next, to induce poisoning by nitrite, the working electrode was immersed in a 125 mM $NaNO_2$ solution. After removing non-chemically adsorbed nitrite by rinsing sequentially with distilled water and the electrolyte (acetate buffer), CV measurements of (1) and (2) were then repeated for the poisoned state. The density of Fe–N_x sites was quantified from the difference between the unpoisoned and poisoned CV profiles.

Based on the baseline region of the N_2-saturated CV, the stripping charge (Q_{strip}) was calculated by eqn (1):

$$Q_{strip}\left[\text{C g}^{-1}\right] = \frac{\text{area[A V]}}{\text{scan rate}\left[\text{V s}^{-1}\right] \times \text{catalyst loading[g]}} \quad (1)$$

where the area corresponds to the difference in baseline nitrogen CV between poisoned and recovery scans between the baseline CVs recorded under N_2 before and after poisoning. The stripping charge was used to calculate the site density (SD) as shown in eqn (2):

$$\mathrm{SD}[\text{sites per g}] = \frac{Q_{\mathrm{strip}}[\mathrm{C\ g^{-1}}] \times N_{\mathrm{A}}[\mathrm{mol^{-1}}]}{n_{\mathrm{strip}} \times F[\mathrm{C\ mol^{-1}}]} \quad (2)$$

where F stands for the Faraday constant and n_{strip} is the number of electrons involved in the reduction of one nitrosyl adsorbed on the metal centers (taken as $n_{\mathrm{strip}} = 5$).

Electrochemical ORR experiments

Electrochemical rotating disk electrode (RDE) experiments were conducted using a Hokuto HZ-Pro potentiostat in conjunction with a BAS RRDE-3A system. All experiments were performed in a standard three-electrode cell (BAS, Catalog No. 013491). A Pt wire (Nilaco, Product No. 351265) and an Ag/AgCl electrode in saturated KCl solution (BAS, Model 013691) served as the counter and reference electrodes, respectively. All potentials were referenced to the reversible hydrogen electrode (RHE) scale using the conversion formula $E_{\mathrm{RHE}} = E_{\mathrm{Ag/AgCl}} + 0.0591 \times \mathrm{pH} + 0.197$ V. The working electrode was a 5 mm-diameter glassy carbon disk electrode enclosed in a PEEK sheath (BAS, Catalog No. 013491; geometric area = 0.196 $\mathrm{cm^2}$). Before electrochemical measurements, the electrode surface was polished to a mirror finish using a wet polishing pad (BAS, MF-1040) with a slurry of Al_2O_3 (0.05 μm) and rinsed with water. For a catalyst loading of 800 μg $\mathrm{cm^{-2}}$, the catalyst ink was prepared by mixing 5 mg of catalyst, 40.8 μL of 5 wt% Nafion solution (Fujifilm Wako, 1-propanol 48 ± 3 wt%, water 45 ± 3 wt%, ethanol <4 wt%). 470 μL of deionized and distilled water, and 470 μL of 2-propanol in an Eppendorf tube. This suspension was sonicated in an ice bath for 30 min. Subsequently, a portion of the ink was drop-cast onto the glassy carbon electrode while rotating at 500–700 rpm using the BAS RRDE system to ensure uniform catalyst deposition. The ORR activity data were collected in an O_2-saturated 0.5 M H_2SO_4 aqueous solution (Sigma-Aldrich, Product No. 28-5940). The catalyst coated on the electrode was activated in an N_2-saturated electrolyte through 8 cyclic voltammetry (CV) scans between 0 and 1.0 V *vs.* RHE at a scan rate of 50 mV $\mathrm{s^{-1}}$ until stable voltammograms were obtained. Subsequently, linear sweep voltammograms (LSVs) were recorded in an O_2-saturated electrolyte between 0 and 1.0 V *vs.* RHE at a scan rate of 1 mV $\mathrm{s^{-1}}$. The measurements were performed at a constant rotation rate of 1700 rpm, using a potential step of 0.02 V and a holding time of 10 s. Background measurements were conducted in N_2-saturated 0.5 M H_2SO_4 to subtract the background current and eliminate the capacitive contributions, thereby isolating the current arising from ORR. ORR activity was evaluated using mass activity calculated from the kinetic current density (J_{kin}) value at 0.8 V *vs.* RHE. The Koutecký–Levich equation was used to calculate the J_{kin} from the geometric current density, J, according to

$$\frac{1}{j} = \frac{1}{j_{\mathrm{lim}}} + \frac{1}{j_{\mathrm{kin}}} \quad (3)$$

where J_{lim} is the diffusion-limited current density, measured at 0.20 V *vs.* RHE. The turnover frequency (TOF) was calculated by using eqn (4).

$$\mathrm{TOF}[\mathrm{s^{-1}}] = \frac{\text{mass activity}[\mathrm{A\ g^{-1}}]}{F[\mathrm{A\ s\ mol^{-1}}] \times \mathrm{SD}[\mathrm{mol\ g^{-1}}]} \quad (4)$$

PEFC MEA preparation and single-cell testing

Preparation of gas diffusion layer (GDL). A mixture of conductive carbon black (Cabot, Vulcan® XC-72) and a PTFE dispersion (Chemours-Mitsui Fluoroproducts Co., Ltd, 10 wt%) was prepared at a solid weight ratio of 3 : 2. The resulting slurry was applied onto a 10 cm × 20 cm carbon paper (AvCarb P50T, AvCarb Material Solutions; hereinafter referred to as CP) using a brush. The coating amount was adjusted to achieve a Vulcan® XC-72 loading of 1.2 mg $\mathrm{cm^{-2}}$ (based on the geometric area of the CP). After coating, the samples were dried in a muffle furnace (Yamato Scientific, FO310) by heating to 350 °C and holding for 1 h to form the GDL.

Preparation and application of catalyst ink. To prepare the catalyst ink for application onto the fabricated GDL, 1080 μL of distilled water and 1374 μL of 2-propanol were first placed in an Eppendorf tube and sonicated at 120 kHz for 5 min. Approximately 60 mg of Fe–N–C catalyst was then further sonicated at 120 kHz for 10 min. Subsequently, 735 μL of 5 wt% Nafion solution (Fujifilm Wako; 1-propanol 48 ± 3 wt%, water 45 ± 3 wt%, ethanol <4 wt%) was introduced, followed by sonication at 120 kHz for 180 min. All sonication steps were performed under ice-cooling conditions. The prepared catalyst ink was repeatedly applied onto a 5 cm × 2.5 cm GDL heated to 55 °C, followed by drying. After achieving an Fe–N–C catalyst loading of 3.5 mg ($\mathrm{cm^{-2}}$)-CP, a mixed solution of 125 mg of 5% Nafion dispersion and 375 mg of 2-propanol was applied onto the surface.

Fabrication of membrane electrode assembly (MEA). A membrane electrode assembly (MEA) was fabricated by hot pressing an assembled stack of a 2.2 cm × 2.2 cm anode electrode, a Nafion membrane (NRE-212, thickness 0.002 inch, Sigma Aldrich), and a 2.2 cm × 2.2 cm cathode electrode at 130 °C for 2 min. The anode electrode utilized a commercial Pt/C catalyst, TEC10E40E (Tanaka Kikinzoku Kogyo, Pt 37 wt%) with a loading of 0.5 mg $\mathrm{cm^{-2}}$. The cathode electrode employed the prepared Fe–N–C catalyst applied at a loading of 3.5 mg $\mathrm{cm^{-2}}$.

Fuel cell performance evaluation. The performance of the MEA was evaluated using a fuel cell testing system and an impedance meter. First, the cell was heated to 80 °C, and humidified N_2 (100% RH) was supplied to both the anode and cathode for approximately 2 h. Subsequently, humidified O_2 was supplied to the cathode and H_2 to the anode at a flow rate of 70 mL $\mathrm{min^{-1}}$, respectively. Polarization curves were obtained by measuring from the open-circuit voltage with a step width of 0.2 A, holding each step for 2 s, until the cell voltage dropped below 0.1 V.

Results and discussion

All MOF materials were pyrolyzed in flowing helium at 1100 °C for 1 h, and the resulting porous structures were characterized by high-resolution Ar adsorption at −187 °C. The Ar adsorption

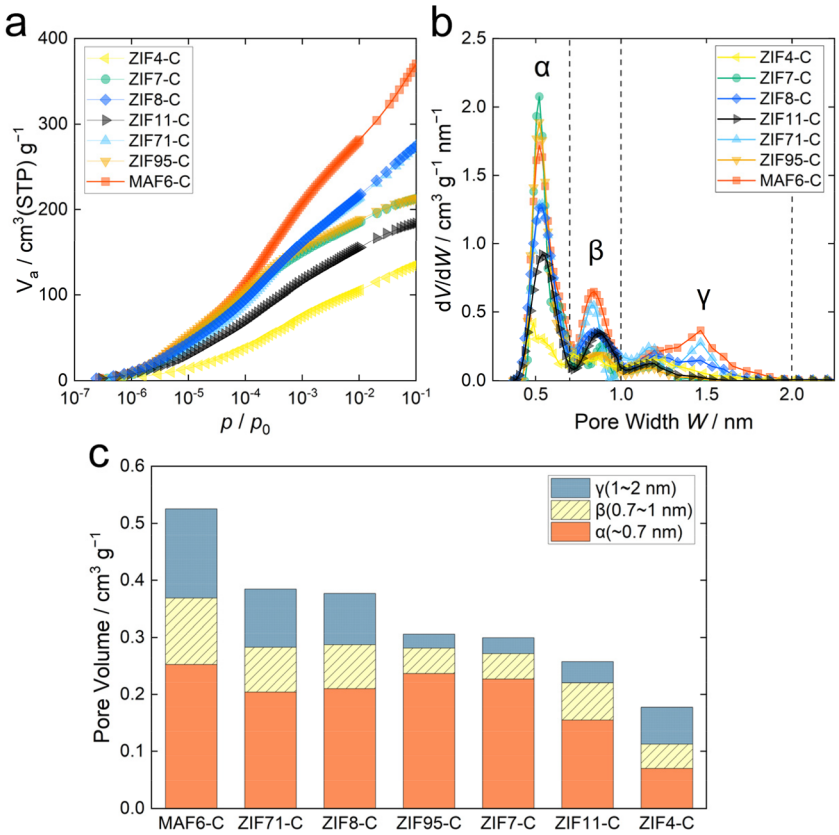

Fig. 2 (a) Ar adsorption isotherms measured at −187 °C for the carbon materials derived from various MOF precursors, plotted on a semi-logarithmic pressure scale to emphasize the low-pressure region associated with micropore filling. (b) Pore-size distributions determined using 2D-NLDFT-HS. (c) Pore volume contributions in distinct pore-size regions (α, W < 0.7 nm; β, 0.7–1.0 nm; γ, 1–2 nm) for the MOF-derived carbons.

isotherms (Fig. 2a) were analyzed using the two-dimensional non-local density functional theory heterogeneous surface (2D-NLDFT-HS) model,[32] which accounts for pore surface heterogeneity and provides micropore size distributions. All carbonized samples (denoted by adding –C after parent MOF name) exhibited dominant micropores across three characteristic regimes, denoted as α (<0.7 nm), β (0.7–1.0 nm), and γ (1–2 nm) (Fig. 2b). The influence of the parent MOF structure was analyzed by quantifying pore-volume contributions in distinct pore-size regimes (Fig. 2c), revealing pronounced differences in β and γ pore fractions. Carbons derived from MAF-6 [30] and ZIF-71 [28] display larger contributions from β and γ pores, consistent with their more open framework structures and larger intrinsic cavities (Table S1), whereas ZIF-4 [1]- and ZIF-11 [1]-derived carbons are characterized by a higher proportion of ultramicropores. These trends indicate partial retention of MOF topology and linker geometry during thermal conversion. When MAF-6 and ZIF-8 samples were pyrolyzed at 500 °C, both materials retained long-range order, as confirmed by powder X-ray diffraction data (Fig. S2), and their pore-size distributions are dominated by narrow peaks centered near the corresponding D_i of the parent MOFs (Fig. S4).

To identify the dominant MOF structural factors governing micropore formation, Pearson correlation coefficients were calculated between the total micropore volume (V_{micro}) of carbonized MOF (MOF-C) samples and multiple precursor descriptors, including the largest free sphere diameter (D_f), the largest included sphere diameter (D_i), cavity-to-window size ratio (D_i/D_f), and metal atom density (Fig. 3a and S5). Among these parameters, D_f exhibited the strongest positive correlation with V_{micro}, whereas D_i is comparatively weak.

During MOF carbonization, imidazolate linkers arranged with finite dihedral angles undergo rotational motion and crosslinking, initiating the formation of the carbon framework.

Consequently, micropore preservation is governed not solely by the pore size metrics (D_f, D_i) and the precursor MOF micropore volume proposed in a previous study[34] but by the spatial proximity of neighboring linkers at the pore aperture. To quantitatively capture this effect, we introduce a geometric descriptor (d_{L-L}) that represents the effective inter-linker distance at the pore opening. This descriptor is derived from a simplified geometric model in which n imidazolate linkers (nMR) define a pore aperture circumscribed by D_f (Fig. 3b). Under this assumption, the inter-linker distance is given by

$$d_{L-L} = D_f \sin\left(\frac{\pi}{n}\right) \quad (5)$$

Using this relation, d_{L-L} values of 1.7 Å (ZIF-8, 6MR), 2.8 Å (MAF-6, 8MR), and 1.2 Å (ZIF-95, 12MR) were obtained.

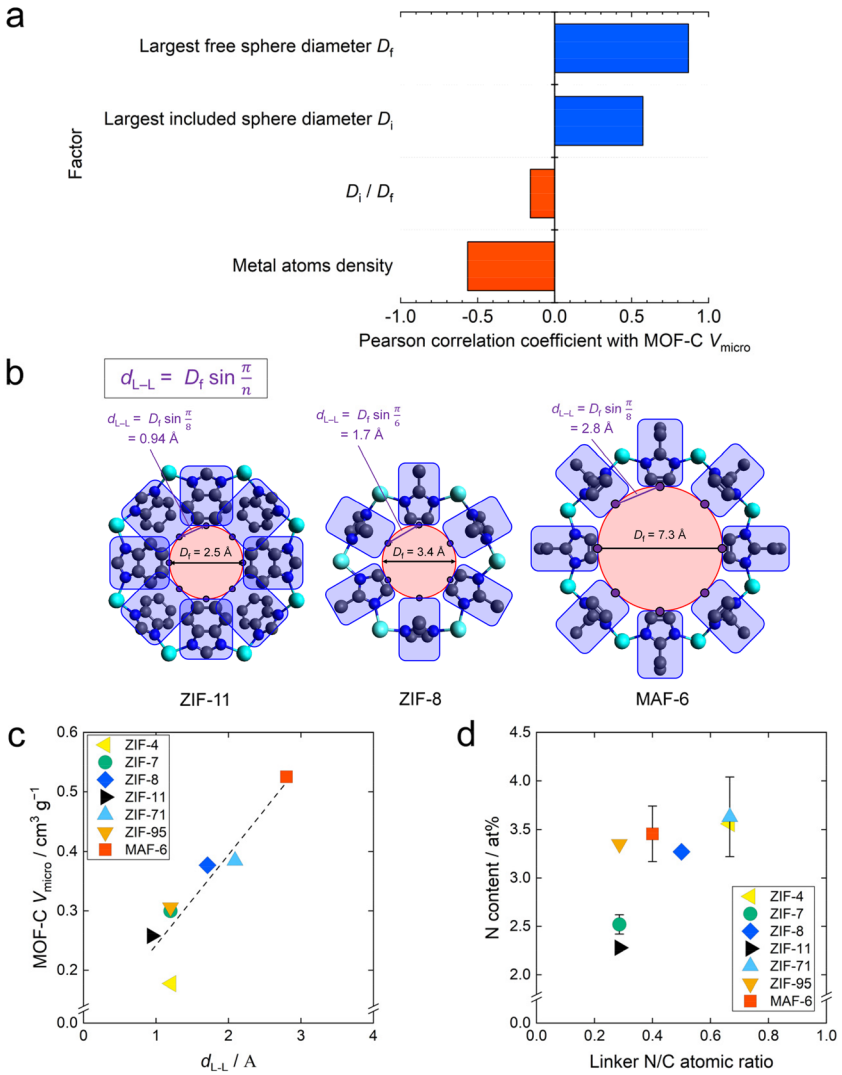

Fig. 3 (a) Pearson correlation coefficients between MOF structural descriptors and the micropore volume (V_{micro}) of carbonized samples (MOF-C). (b) Definition of the geometric descriptor d_{L-L}, representing the effective inter-linker distance at the pore aperture. (c) Correlation between d_{L-L} of V_{micro} of MOF-C samples. (d) Relationship between linker N/C ratio and nitrogen content. For samples shown with error bars, measurements were performed twice, and the average values are plotted.

Although some d_{L-L} values were smaller than a C–C single bond (~1.5 Å), this reflects projection of three-dimensionally twisted linkers onto a two-dimensional plane, consistent with linker rotation during carbonization. A markedly stronger correlation is observed between d_{L-L} and V_{micro} (Fig. 3c) than for conventional pore descriptors, indicating that shorter inter-linker distances promote linker condensation, whereas larger distances favor micropore retention.

Nitrogen atoms present in the precursor MOFs are indispensable for the formation of catalytically active Fe–N_x sites in Fe–N–C catalysts. Accordingly, the nitrogen content of carbonized MOF precursors (MOF-C) was quantified by X-ray photoelectron spectroscopy (XPS) (Table S2) and compared with the nitrogen-to-carbon atomic ratio of the parent imidazole linker (Linker N/C) (Fig. 3d).

MOFs with higher linker N/C ratios generally tend to retain larger amounts of nitrogen after carbonization, increasing the availability of nitrogen species for Fe coordination, although the correlation is moderate (Pearson $r = 0.72$) and nitrogen retention is also influenced by other factors. The deviation observed for some samples, such as ZIF-95-C—which retains a comparable nitrogen content (3.35 at%) despite the lowest linker N/C ratio (0.29)—indicates that nitrogen retention is not governed solely by linker stoichiometry, but also other factors such as framework topology, ring size, metal-node density, and pyrolysis kinetics. Previous studies have proposed a thermally driven Fe–N_x site formation mechanism, in which iron oxide nanoparticles or clusters derived from Fe precursors initially form within micropores and subsequently release atomic Fe species during heat treatment (Fig. 4a);[16,31,35] these mobile Fe species diffuse through the pore network and are trapped at nitrogen-doped sites to generate Fe–N_x moieties. Consistent with this mechanism, a correlation between micropore volume and Fe–N_x site density has been reported across Fe–N–C.[36,37]

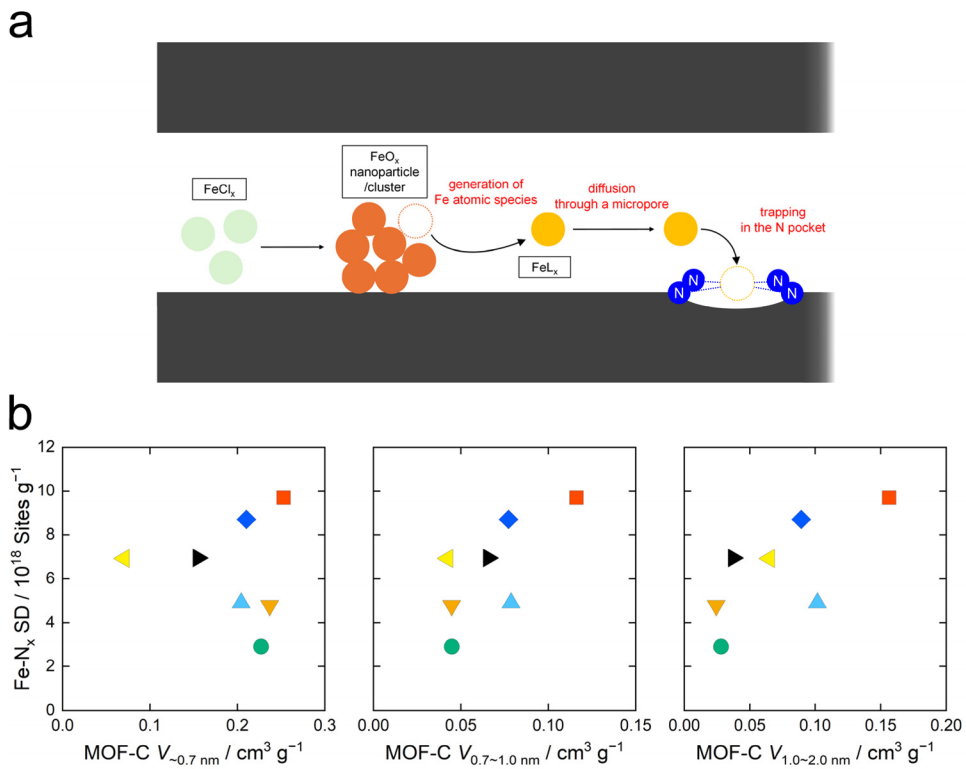

Fig. 4 (a) Schematic illustration of the Fe–N_x site-formation mechanism during thermal treatment of Fe-loaded MOF-C.[31,35] (b) Relationship between micropore volume in different pore-size regimes (a, pore width $W < 0.7$ nm; b, $0.7 \leq W < 1.0$ nm; c, $W \geq 1.0$ nm) and the Fe–N_x site density (SD) of the corresponding Fe–N–C catalysts.

Following a literature approach,[31] Fe–N–C catalysts were synthesized by impregnating MOF-derived carbons (MOF-C) with $FeCl_3$ in 2-propanol, followed by drying and thermal activation at 700 °C in flowing helium. To quantify Fe–N_x site density (SD) of synthesized Fe–N–C catalysts, we used electrochemical reductive stripping of NO derived from nitrite (NO_2^-).[33,36] Because this method probes electrochemically accessible Fe–N_x sites, contributions from any metallic Fe or Fe_3C phases are not expected to be counted as Fe–N_x sites. The two-step synthesis used here, in which Fe is introduced to the pre-formed carbon by thermal activation at 700 °C rather than by co-pyrolysis with the carbon precursor, further limits the formation of such phases. Bulk Fe content and the corresponding Fe utilization, defined as the fraction of bulk Fe present as Fe–N_x sites, are summarized in Table S3. Notably, SD increases nearly linearly with micropore volumes in the 0.7–2 nm range (Fig. 4b). In contrast, SD shows no correlation with the total nitrogen content or nitrogen speciation (Fig. S8), presumably because nitrogen atoms are present in excess relative to Fe–N_x (see Tables S2–S4). These results indicate that

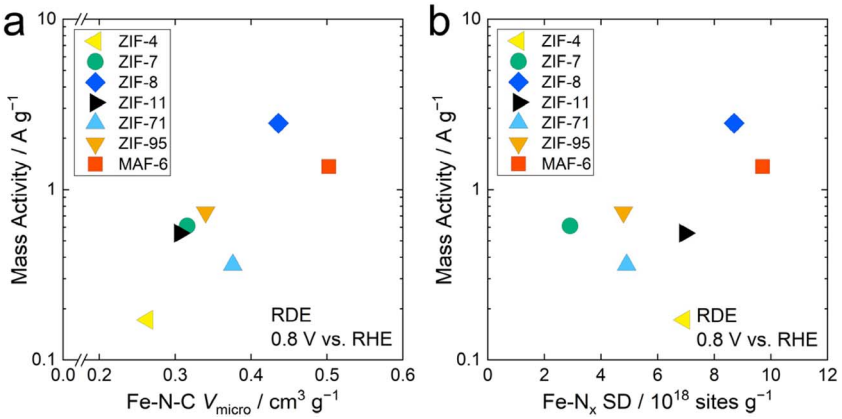

Fig. 5 Mass activity of Fe–N–C catalysts as a function of (a) the micropore volume (V_{micro}) and (b) Fe–N_x site-density, determined from ORR experiments performed in O_2-saturated 0.5 M H_2SO_4 electrolyte at 25 °C in a three-electrode cell equipped with a rotating disc electrode. Activities were calculated from the kinetically controlled current density at 0.8 V *vs.* RHE.

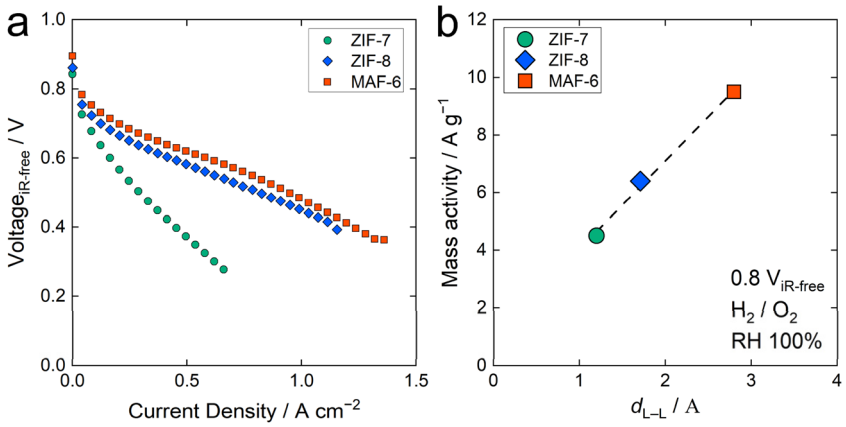

Fig. 6 (a) Polarization curves of the Fe–N–C catalysts derived from MAF-6, ZIF-8, and ZIF-7 measured using a PEFC single cell operated at 80 °C with H_2 and O_2 feeds at 100% relative humidity (RH). Cathode: Fe–N–C, 4 mg cm^{-2}; anode: Pt/C, 0.1 mg cm^{-2}. (b) Mass activity determined at 0.8 V *vs.* RHE.

micropores larger than ~0.7 nm play a decisive role in Fe–N_x site formation, highlighting the importance of selecting MOFs that yield high micropore volumes in this size regime (Fig. 2 and 4).

To investigate the roles of microporosity and Fe–N_x site density in ORR performance of the synthesized Fe–N–C catalysts, electrochemical ORR experiments were conducted in O_2-saturated H_2SO_4 electrolyte at 25 °C. The mass activity was calculated from the kinetic current density at 0.8 V *vs.* reversible hydrogen electrode (RHE) using linear sweep voltammetry (LSV) (Fig. S9). The mass activity increases with micropore volume (V_{micro}), indicating that the Fe–N_x sites responsible for ORR are predominantly located within micropores (Fig. 5a), consistent with the trends in Fig. 4. In contrast, although mass activity generally increases with SD, a noticeable scatter is observed (Fig. 5b), indicating that SD alone does not account for activity trends and that additional electronic factors modulate the intrinsic activity of Fe–N_x sites. The site-normalized activity (TOF) calculated from the half-cell data does not correlate with V_{micro} and Fe–N_x site density, N content of MOF-derived carbons, or d_{L-L} (Fig. S10), confirming that the descriptor d_{L-L} captures structure encoding in controlling micropore formation and Fe–N_x site density but does not encompass the electronic factors that govern intrinsic per-site activity.

As a practically relevant performance evaluation, Fe–N–C catalysts derived from MAF-6, ZIF-8, and ZIF-7 were evaluated in a PEFC single cell at 80 °C. The MAF-6-derived Fe–N–C catalyst, which possesses the largest V_{micro}, exhibited *I–V* characteristics exceeding those of the ZIF-8-derived catalyst (Fig. 6a). Furthermore, comparison of the mass activity in the reaction-limited region (at 0.8 V *vs.* RHE) reveals that the activity increases with V_{micro} and consequently the geometric descriptor d_{L-L} (Fig. 6b).

In this study, we identify the geometric descriptor d_{L-L} as a key structure-encoding parameter that links MOF pore-aperture geometry to catalysis-relevant carbon properties in MOF-derived Fe–N–C catalysts. Derived from the pore-aperture diameter (D_f) and the number of imidazolate linkers defining the framework opening, d_{L-L} quantitatively captures the spatial proximity of linkers that govern micropore evolution during carbonization. By correlating micropore volume, Fe–N_x site density, ORR mass activity, and PEFC single-cell performance, we establish a quantitative structure–property–function relationship that enables rational precursor selection.

The descriptor d_{L-L} allows efficient screening of promising precursor MOFs from large structural databases using simple geometric criteria, as exemplified by the identification of highly promising candidates such as ZIF-70 [28,38] (Table S5), and is readily compatible with emerging high-throughput screening approaches.[39] Importantly, the structure-encoding framework introduced here is general and extendable to a broad class of metal–N–C (M–N–C) catalysts that share analogous active-site formation mechanisms (*e.g.*, Cu- and Pd-based M–N–C catalysts[11,12]), providing a precursor-level strategy for accelerating catalyst discovery and design within the broader and rapidly expanding class of atomically dispersed supported metal catalysts.[40]

Conclusions

In summary, the parent MOF structure encodes the catalysis-relevant properties of the derived Fe–N–C catalyst. The results show that framework geometry governs micropore evolution during carbonization, and that this microporosity in turn controls Fe–N_x site density and ORR mass activity. In particular, the geometric descriptor, d_{L-L}, captures the linker proximity at the pore aperture and provides a direct structure-level predictor of the microporous carbon characteristics that underpin catalytic performance. These findings establish a structure–property–function relationship connecting parent MOF geometry, carbon pore properties, active-site formation, and electrochemical performance. Furthermore, more promising precursor candidates can be readily screened from MOF databases using simple geometric criteria. More broadly, the structure-encoding framework introduced here is generalizable to a broad class of M–N–C catalysts that share analogous

thermally driven active-site formation mechanisms, providing a precursor-level strategy for accelerating catalyst discovery and design.

Author contributions

D. H. wrote the initial draft. I. O. assisted with writing the original draft. P. C. carried out Ar physisorption. P. C., S. M., and I. O. provided supervision, and revised and edited the manuscript.

Conflicts of interest

There are no conflicts to declare.

Data availability

The data supporting this article have been included as part of the supplementary information (SI). Supplementary information: additional experimental details and methods, full characterization data, additional experimental results, and the list of promising MOF candidates identified in this study. See DOI: https://doi.org/10.1039/d6ta02641a.

Acknowledgements

The authors thank the staff members (Drs Takeda and Sawasato) at the Global Facility of Hokkaido University for ICP analysis. I. O. acknowledges Iwatani Naoji Foundation for the financial support. A part of this work was conducted at Joint-use Facilities: Laboratory of Nano–Micro Material Analysis, Hokkaido University, supported by Nano-technology Platform Program of the Ministry of Education, Culture, Sports, Science and Technology (MEXT), Japan. P. C. acknowledges Mr Huang Jyun Wu for gas sorption analysis which is supported by National Science and Technology Council (114-2113-M-001-025) and Academia Sinica (AS-iMATE-114-23).

References

1 K. S. Park, Z. Ni, A. P. Côté, J. Y. Choi, R. Huang, F. J. Uribe-Romo, H. K. Chae, M. O'Keeffe and O. M. Yaghi, *Proc. Natl. Acad. Sci. U. S. A.*, 2006, **103**, 10186–10191.
2 E. Proietti, F. Jaouen, M. Lefevre, N. Larouche, J. Tian, J. Herranz and J. P. Dodelet, *Nat. Commun.*, 2011, **2**, 416.
3 T. Asset, F. Maillard and F. Jaouen, *Supported Metal Single Atom Catalysis*, 2022, pp. 531–582, DOI: 10.1002/9783527830169.ch13.
4 M. Gong, A. Mehmood, B. Ali, K. W. Nam and A. Kucernak, *ACS Catal.*, 2023, **13**, 6661–6674.
5 S. Specchia, P. Atanassov and J. H. Zagal, *Curr. Opin. Electrochem.*, 2021, **27**, 100687.
6 A. Pedersen, A. Bagger, J. Barrio, F. Maillard, I. E. L. Stephens and M. M. Titirici, *J. Mater. Chem. A*, 2023, **11**, 23211–23222.
7 F. Luo, S. Wagner, W. Ju, M. Primbs, S. Li, H. Wang, U. I. Kramm and P. Strasser, *J. Am. Chem. Soc.*, 2022, **144**, 13487–13498.
8 J. Li, W. Xia, X. Xu, D. Jiang, Z. X. Cai, J. Tang, Y. Guo, X. Huang, T. Wang, J. He, B. Han and Y. Yamauchi, *J. Am. Chem. Soc.*, 2023, **145**, 27262–27272.
9 J. S. Bates, F. Khamespanah, D. A. Cullen, A. A. Al-Omari, M. N. Hopkins, J. J. Martinez, T. W. Root and S. S. Stahl, *J. Am. Chem. Soc.*, 2022, **144**, 18797–18802.
10 J. Cui, W. Zhang, Y. Hou, X. Yang, Y. Gao, X. Zhang, C. Fang, Y. Yang, Z. Li, B. Liu and J. Zhu, *J. Am. Chem. Soc.*, 2026, **148**, 665–676.
11 Y. Qu, Z. Li, W. Chen, Y. Lin, T. Yuan, Z. Yang, C. Zhao, J. Wang, C. Zhao, X. Wang, F. Zhou, Z. Zhuang, Y. Wu and Y. Li, *Nat. Catal.*, 2018, **1**, 781–786.
12 S. Wei, A. Li, J. C. Liu, Z. Li, W. Chen, Y. Gong, Q. Zhang, W. C. Cheong, Y. Wang, L. Zheng, H. Xiao, C. Chen, D. Wang, Q. Peng, L. Gu, X. Han, J. Li and Y. Li, *Nat. Nanotechnol.*, 2018, **13**, 856–861.
13 Y. Chen, R. Zhang, Z. Chen, J. Liao, X. Song, X. Liang, Y. Wang, J. Dong, C. V. Singh, D. Wang, Y. Li, F. D. Toste and J. Zhao, *J. Am. Chem. Soc.*, 2024, **146**, 10847–10856.
14 Y. Zeng, C. Li, B. Li, J. Liang, M. J. Zachman, D. A. Cullen, R. P. Hermann, E. E. Alp, B. Lavina, S. Karakalos, M. Lucero, B. Zhang, M. Wang, Z. Feng, G. Wang, J. Xie, D. J. Myers, J.-P. Dodelet and G. Wu, *Nat. Catal.*, 2023, **6**, 1215–1227.
15 A. Sarapuu, J. Lilloja, S. Akula, J. H. Zagal, S. Specchia and K. Tammeveski, *ChemCatChem*, 2023, **15**, e202300849.
16 S. Liu, C. Li, M. J. Zachman, Y. Zeng, H. Yu, B. Li, M. Wang, J. Braaten, J. Liu, H. M. Meyer, M. Lucero, A. J. Kropf, E. E. Alp, Q. Gong, Q. Shi, Z. Feng, H. Xu, G. Wang, D. J. Myers, J. Xie, D. A. Cullen, S. Litster and G. Wu, *Nat. Energy*, 2022, **7**, 652–663.
17 T. Murakami, Y. Yamazaki, A. Okada, S. R. Mukai and I. Ogino, *Catal. Today*, 2025, **455**, 115304.
18 H. Xu, R. Li, Y. Li, X. Lu, H. Liu, P. Yang and J. Bai, *J. Mater. Chem. A*, 2025, **13**, 13675–13692.
19 H. Choi, S. J. Shin, G. Bae, J. Cho, M. H. Han, M. T. Sougrati, F. Jaouen, K. S. Lee, H. S. Oh, H. Kim and C. H. Choi, *J. Am. Chem. Soc.*, 2025, **147**, 13220–13228.
20 A. Okada, D. Homma, T. Murakami, S. R. Mukai and I. Ogino, *Ind. Eng. Chem. Res.*, 2026, **65**, 6848–6860.
21 J. Liu, Y. Liu, B. Nan, D. Wang, C. Allen, Z. Gong, G. He, K. Fu, G. Ye and H. Fei, *Angew. Chem., Int. Ed.*, 2025, **64**, e202425196.
22 T. Sato, N. Hayashida, D. Homma, A. Okada, S. R. Mukai and I. Ogino, *Chem. Eng. J.*, 2026, **540**, 177377.
23 Z. Zheng, Z. Rong, H. L. Nguyen and O. M. Yaghi, *Inorg. Chem.*, 2023, **62**, 20861–20873.
24 Z. Zheng, N. Rampal, T. J. Inizan, C. Borgs, J. T. Chayes and O. M. Yaghi, *Nat. Rev. Mater.*, 2025, **10**, 369–381.
25 J. Yang, Y.-B. Zhang, Q. Liu, C. A. Trickett, E. Gutiérrez-Puebla, M. Á. Monge, H. Cong, A. Aldossary, H. Deng and O. M. Yaghi, *J. Am. Chem. Soc.*, 2017, **139**, 6448–6455.
26 Z. Levell, S. Yu, R. Wang and Y. Liu, *J. Am. Chem. Soc.*, 2025, **147**, 603–609.
27 Y. Huang, Y. Chen, M. Xu, A. Ly, A. Gili, E. Murphy, T. Asset, Y. Liu, V. De Andrade, C. U. Segre, A. L. Deriy, F. De Carlo,

M. Kunz, A. Gurlo, X. Pan, P. Atanassov and I. V. Zenyuk, *Mater. Today*, 2023, **69**, 66–78.
28 R. Banerjee, A. Phan, B. Wang, C. Knobler, H. Furukawa, M. O'Keeffe and O. M. Yaghi, *Science*, 2008, **319**, 939–943.
29 B. Wang, A. P. Cote, H. Furukawa, M. O'Keeffe and O. M. Yaghi, *Nature*, 2008, **453**, 207–211.
30 X. C. Huang, Y. Y. Lin, J. P. Zhang and X. M. Chen, *Angew. Chem., Int. Ed.*, 2006, **45**, 1557–1559.
31 J. Li, H. Zhang, W. Samarakoon, W. Shan, D. A. Cullen, S. Karakalos, M. Chen, D. Gu, K. L. More, G. Wang, Z. Feng, Z. Wang and G. Wu, *Angew. Chem., Int. Ed.*, 2019, **58**, 18971–18980.
32 J. Jagiello, J. Castro-Gutierrez, R. L. S. Canevesi, A. Celzard and V. Fierro, *ACS Appl. Mater. Interfaces*, 2021, **13**, 49472–49481.
33 D. Malko, A. Kucernak and T. Lopes, *Nat. Commun.*, 2016, **7**, 13285.
34 V. Armel, S. Hindocha, F. Salles, S. Bennett, D. Jones and F. Jaouen, *J. Am. Chem. Soc.*, 2017, **139**, 453–464.
35 J. Li, L. Jiao, E. Wegener, L. L. Richard, E. Liu, A. Zitolo, M. T. Sougrati, S. Mukerjee, Z. Zhao, Y. Huang, F. Yang, S. Zhong, H. Xu, A. J. Kropf, F. Jaouen, D. J. Myers and Q. Jia, *J. Am. Chem. Soc.*, 2020, **142**, 1417–1423.
36 M. Primbs, Y. Sun, A. Roy, D. Malko, A. Mehmood, M.-T. Sougrati, P.-Y. Blanchard, G. Granozzi, T. Kosmala, G. Daniel, P. Atanassov, J. Sharman, C. Durante, A. Kucernak, D. Jones, F. Jaouen and P. Strasser, *Energy Environ. Sci.*, 2020, **13**, 2480–2500.
37 F. Jaouen, M. Lefèvre, J.-P. Dodelet and M. Cai, *J. Phys. Chem. B*, 2006, **110**, 5553–5558.
38 R. Banerjee, H. Furukawa, D. Britt, C. Knobler, M. O'Keeffe and O. M. Yaghi, *J. Am. Chem. Soc.*, 2009, **131**, 3875–3877.
39 Z. Rong, Z. Chen, F. Luong, S. Chheda, H. T. N. Luong, Z. Zheng, K. Greco, A. A. Alghamdi, K. H. Bui, T. Jaffrelot Inizan, T. Nguyen-Dang, H. H. Pham, D. D. Le, J. Sauer, V. B. T. Phung, J. T. Chayes, C. Borgs, M. Boley, L. El Ghaoui and O. M. Yaghi, *Nat. Synth.*, 2026, **5**, 409–419.
40 B. C. Gates, M. Flytzani-Stephanopoulos, D. A. Dixon and A. Katz, *Catal. Sci. Technol.*, 2017, **7**, 4259–4275.

